Nanoscale

Encapsulated MAPbBr3 in nickel oxide nanotubes and their electroluminescence

Journal:	*Nanoscale*
Manuscript ID	NR-ART-01-2022-000019.R1
Article Type:	Paper
Date Submitted by the Author:	01-Apr-2022
Complete List of Authors:	Gonzalez Rodriguez, Roberto; University of North Texas, Physics Hathaway, Evan; University of North Texas, Physics Lin, Yuankun; University of North Texas, Physics Coffer, Jeffery; Texas Christian University, Chemistry Cui, Jingbiao; University of North Texas, Physics

ARTICLE

Encapsulated $MAPbBr_3$ in nickel oxide nanotubes and their electroluminescence

Received 00th January 20xx,
Accepted 00th January 20xx

DOI: 10.1039/x0xx00000x

*Roberto Gonzalez-Rodriguez[1], Evan Hathaway[1], Yuankun Lin[1], Jeffery L. Coffer[2], and Jingbiao Cui[1]**

Metal halide perovskites have emerged as the next generation of light emitting semiconducting materials due to their excellent properties such as tunable bandgaps, high photoluminescence quantum yield, and high color purity. Nickel oxide is a hole transport material that has been used in planar light emitting diodes (LEDs). In this paper, we develop a novel method for the large scale fabrication of metal halide perovskite nanowire arrays encapsulated inside nickel oxide nanotubes. We study the structural and spectral properties of these infiltrated perovskites nanowires and, to the best of our knowledge, for the first time report on a working LED device consisting of perovskites encapsulated inside nickel oxide nanotubes. Finally, we study the photoluminescence and electroluminescence of an LED with $MAPbBr_3$ inside nickel oxide nanotubes and obtain an outstanding current efficiency of 5.99 Cd/A and external quantum efficiency of 3.9% for the LED device.

1. Introduction

Metal halide perovskites $MAPbX_3$ (X=Cl, Br, I and $MA=CH_3NH_3$) have attracted much attention in recent years due to a number of favorable intrinsic properties: a relatively large absorption coefficient, low exciton binding energy, high charge-carrier mobility, and high dielectric constant,[1] which make this class of materials ideal for various applications in photovoltaics, light emitting diodes (LEDs), lasers, and photodetectors.[2-5] One advantage of using perovskites in the aforementioned applications is their low cost and processability as compared to established inorganic semiconductors such as Si and GaN which are widely used in current devices.[6, 7] Thus the potential use of pervoskites in such platforms could have a significant impact on the electronics and optoelectronics markets. For example, perovskite-based photodetectors could be used in video imaging,[8] optical communications,[9] and biological/chemical sensing.[10, 11] Perovskite semiconductors have a direct band-gap that is sensitive to halide identity, offering a great opportunity for the tuning of device functionality in order to meet different needs.[12, 13]

One challenge in achieving competitive device performance is the search for a suitable p-type semiconductor which would serve to both stabilize the perovskites and form heterojunctions in the fabricated functional device. In this study, we take an initial step to encapsulate perovskite materials in nickel oxide (NiO_x) nanotubes for LED applications. We choose NiO_x for several reasons: (a) it has high carrier mobility, good stability and processability;[14] (b) it is an inorganic p-type metal oxide and hole transport material, in the same family as tungsten oxide and vanadium oxide. In fact, NiO_x has been successfully used as a hole transport layer in thin film and nanocrystalline perovskite based solar cells and LEDs with planar configurations, in inverted solar cell devices,[15-17] and in tandem c-Si solar cells integrated with perovskite solar cells;[18] (c) as an inorganic metal oxide used for hole transport materials, NiO_x has the advantage over the organic counterpart PEDOT:PSS which is highly hygroscopic and acidic and causes damage the conductive glasses such as FTO and ITO as well the perovskites; (d) furthermore, NiO_x matches the perovskite's energy level making it ideal for use in perovskite-based LEDs.

In addition to forming a heterojunction with the encapsulated perovskite, the porous NiO layer also serves to protect the perovskite from degradation in moist aqueous environments, which is a major issue in the practical widespread development of perovskite-based devices. To date, great effort has been expended to improve the long-term stability of perovskites.[19] One such strategy is to isolate the perovskites in porous materials. This has the added benefit of improving the phase stability of the imbedded perovskites, [20] as demonstrated with the retention of the cubic phase of the perovskite $MAPbI_{2.25}Br_{0.75}$ when the material was formed in porous Si nanotubes.[21] Other porous nanomaterials, such as porous alumina and mesoporous silica, have been reported to serve as templates for perovskite deposition and size control, with an associated improvement in long-term stability. To our knowledge, the formation and properties of perovskites inside NiO nanotubes and their applications in solar cells and LEDs has yet to be reported.

[1] *Department of Physics, University of North Texas, Denton, Texas, 76203, USA*
[2] *Department of Chemistry and Biochemistry, Texas Christian University, TCU Box 298860, Fort Worth, Texas, 76129, USA*
[a]

** Corresponding author*
E-mail: jingbiao.cui@unt.edu

In this paper, we study the fabrication of nickel oxide nanotubes for the confinement of the perovskite $MAPbBr_3$ and demonstrate their LED performance. We show that the length, inner diameter, and tube wall thickness of NiOx nanotubes can be controlled through the tuning of the deposition parameters and ZnO nanowire template. Furthermore, we study the morphological, photoluminescent (PL), and electroluminescent (EL) properties of $MAPbBr_3$ encased in porous NiO nanotubes. The LED devices show a promising green light emission under various applied voltages. This research shows potential for the fabrication of stable perovskite-based LED devices and opens a great opportunity for the fabrication of nano-LEDs using individual encapsulated perovskite nanowires.

2. Results and Discussion

Porous nickel oxide nanotubes were prepared using ZnO nanowire arrays as a sacrificial template (see detailed fabrication procedures in Supporting Information Figure S1). The nanotube length and inner diameter are defined by the dimensions of the template and the thickness of the nanotube wall is controlled by the nickel deposition time. In our previous work, we reported that the dimensions of the ZnO nanowires can be tuned from 150 nm up to 4 µm in length, and from 30 nm up to 200 nm in diameter.[21] In this study we selected ZnO nanowire template arrays with a diameter of 100 ± 30 nm as shown by the cross-sectional SEM images of Figure S3. The process for the formation of NiO NTs includes the immersion of ZnO nanowire arrays in a nickel chloride solution, which allows for the adsorption of Ni^{2+} onto the ZnO surface. This is then followed by a hydrolysis step, which liberates H^+ and forms $Ni(OH)_2$ according to the following equation:

$$Ni^{2+} + 2H_2O \rightarrow Ni(OH)_2 + 2H^+ \quad (1)$$

During this process, ZnO/$Ni(OH)_2$ core-shell nanowires are formed. Note that ZnO nanowires may be partially dissolved in the presence of H^+, and as such, the fabrication of thicker $Ni(OH)_2$ shells leads to a slightly reduced inner diameter. This means that for longer deposition times the nickel oxide shell thickness becomes more obvious due to the double growth from both the inside and outside of the shell. In order to remove the ZnO core, the sample was immersed in diluted sodium hydroxide solution and rinsed several times with DI water. At this point, a tubular structure of $Ni(OH)_2$ is obtained. In order to convert these into nickel oxide nanotubes, the $Ni(OH)_2$ tubes were annealed at a high temperature of 500 °C, then washed with a 1% HCl solution, after which they were annealed again in air at 500 °C. After this step, $pNiO_x$ NTs are finally obtained (**Figure 1**).

The shell thickness of NiO_x NTs can be tuned by controlling the nickel hydrolysis time. Figures 1a-e show the characteristic SEM images of $pNiO_x$ NTs obtained for different nickel deposition times ranging from 10 min up to 3 hours. A 10 min deposition time resulted in the incomplete formation of a thin NiO_x layer on the substrate. However, increasing Ni^{2+} deposition times to 30 min and beyond resulted in a tubular morphology associated with $pNiO_x$. Figure 1f shows the change of shell thickness versus reaction time. One can see that the shell thickness increases from 13.7 nm for a 30 min nickel deposition time to 44.6 nm for one lasting 3h, indicating longer deposition times lead to thicker NiO_x shell walls. Figure 1g shows TEM images of $pNiO_x$ NTs obtained at different nickel deposition times. Note that the $pNiO_x$ shell walls are very thin and fragile for samples with 30 min deposition times, and as such the NTs were partially destroyed during the TEM sample preparation. In order to further confirm the tubular structure, TEM-EDX line scans were performed for nanotubes with deposition times of 1, 2 and 3 h (Figure S5). These line scans show a double hump shaped composition distribution for nickel and oxygen due to the NT walls. This type of compositional change is a typical characteristic of nanotubes. The actual composition of Ni and O were found to be 39.98 at% and 60.02 at%, respectively. Figure 1h shows a higher magnification TEM image for the pNiOx NTs grown for 1 h. In these images it is possible to observe a highly porous structure for these tubes, similar to that observed for SiNTs. These pores were likely formed due to an Ostwald type coalescence during the annealing process. The lattice spacing which corresponds to the (200) plane of NiO, d = 0.207 nm, was measured using a high-resolution TEM (HRTEM). The corresponding Fast Fourier Transform (FFT) is also shown in Figure 1i, indicating the nanotube has a polycrystalline structure. The lattice spacing, d=0.244 nm, that corresponds to the (111) plane is also observed and is shown in Figure S4.

Figure 2a shows the X-ray diffraction (XRD) patterns recorded for pNiOx NTs with different nickel deposition times of 1, 2, and 3 h. The XRD pattern from the FTO glass substrate is also shown in this figure for reference. Two peaks with maxima centered at 2Θ = 37.14 and 43.35° were observed, which correspond to the (111) and (200) planes of cubic NiO, respectively. The XRD data confirm the observations obtained in the HRTEM measurements. One can see that the increase of wall thickness in $pNiO_x$ NTs as a result of the increased growth time of nickel leads to the increase of the XRD intensity of (111) peak.

X-ray photoelectron spectroscopy (XPS) was used to obtain more detail about the chemical composition of the $pNiO_x$ NTs. Figure 2b shows the high resolution XPS analysis for Ni 2p 3/2. It shows two peaks at 853.7 and 855.5 eV, which correspond to Ni^{2+} and Ni^{3+}.[22, 23] A satellite peak around 860 eV was also observed and is known as a shake-up peak in NiO_x. This peak appears at a higher binding energy of the Ni $2p_{3/2}$ and Ni $2p_{1/2}$ region and originates from a mixture of d-d transition and enhancement of Ni_{3d}—O_{2p} hybridization. The peak for Ni^{2+} is due to the standard rock salt cubic form of Ni-O bonding and the Ni^{3+} is due to some vacancies which are present in the structure.[24, 25] Figure 2c shows the high resolution XPS for O 1s. Two peaks are observed at 529.4 eV and 531.3 eV, respectively. The first one (O_1) corresponds to the O anions in NiO lattice and the second (O_2) is absorbed oxygen ions in the vicinity of Ni vacancies.[26] Both XRD and XPS studies show that the ZnO template was completely removed from the $pNiO_x$ NTs.

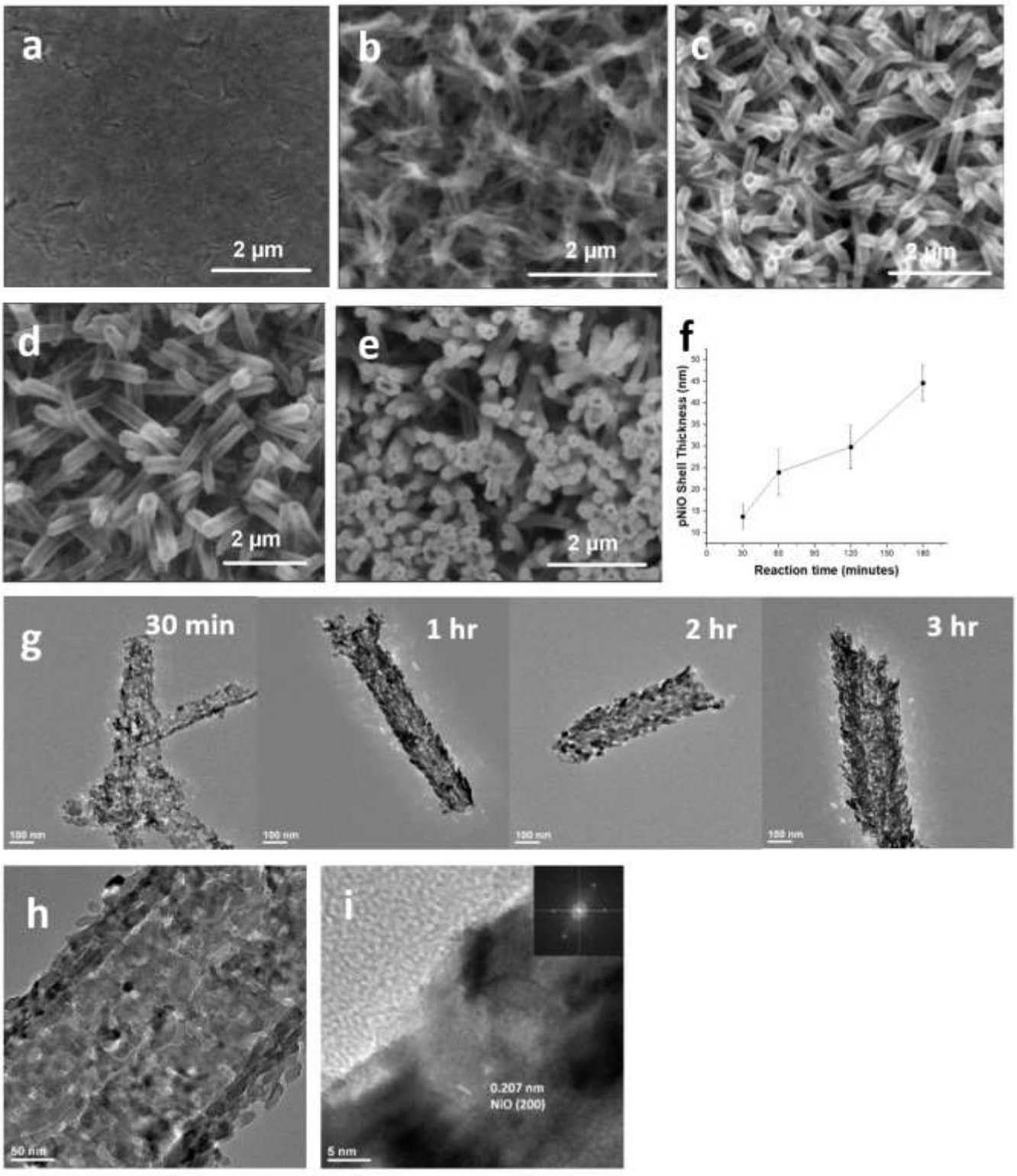

Figure 1. SEM of pNiO NTs at different nickel deposition times: a) 10 min, b) 30 min, c) 1 h, d) 2 h, and e) 3 h; f) pNiO tube wall thickness versus reaction time; g) TEM of pNiO NTs at different Nickel deposition times; h) TEM image of porous structure in pNiO NTs; i) HRTEM of pNiO NTs showing the polycrystalline domains with the corresponding FFT in the inset.

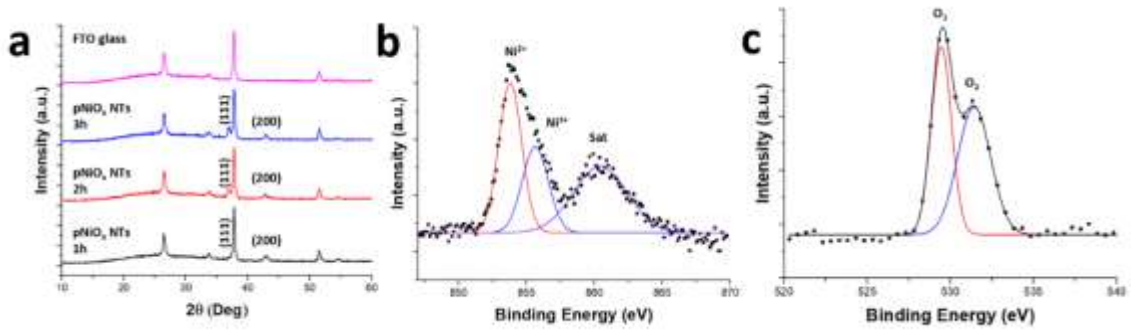

Figure 2. a) XRD of pNiO$_x$ NTs on FTO glass; b) High resolution XPS spectra for Ni 2p; and c) High resolution XPS spectra for O 1s. The solid lines in b) and c) are deconvolution fittings to the experimental data using Gaussian function.

Formation of $MAPbBr_3$ nanowires were achieved by the immersion of the pNiO$_x$ NTs in perovskite's precursors, followed by spin coating at 6000 rpm to remove any excess perovskite precursors on the surface, leaving the precursor inside the pNiO$_x$ NTs only. Finally, the samples were baked at 95 °C in order to evaporate the solvent leaving perovskites nanowires inside the tubes. Figure S1 provides a visualization of the process. The pNiOx NTs with different nickel deposition times (30 min, 1, 2h, and 3h) were loaded with perovskites. However, the perovskites inside pNiO$_x$ NTs with a nickel deposition time of 30 min do not have a well-defined tubular structure. Instead, a $MAPbBr_3$/pNiO$_x$ NTs composite hybrid is obtained as shown by the SEM image in (S6). In the case of $MAPbBr_3$ in pNiOx NTs with 1, 2 and 3 h nickel deposition time, a well-defined core-shell structure is observed as shown by SEM images in **Figure 3a.** The corresponding cross-section SEM images can be found in Figure S7a. The TEM images of perovskite inside nickel oxide are shown in Figure S8. Note that no perovskite material was found outside of the pNiO$_x$ NTs. Figure 3b (left) shows the TEM image of $MAPbBr_3$ inside pNiO$_x$ NTs. The perovskite is seen as a dark core wrapped by a thin pNiOx shell, confirming the perovskite nanowires formed inside the pNiOx NTs. The TEM-EDX line scan for the $MAPbBr_3$/pNiOx NT is also shown in Figure 3b (right). The double hump peaks for nickel and oxygen elements indicate the tubular structures of pNiOx NTs. Between these double humps, strong signals for lead and bromide are observed, suggesting the successful loading and formation of perovskite inside the nanotubes. As mentioned above, the sidewall of the pNiOx tube contains a porous structure which allows for the infiltration of the perovskite precursor into the nanotube, forming a uniform perovskite nanowire (see more details in the TEM-EDX mapping of Figure S9). Figure 3c shows the HRTEM image of $MAPbBr_3$ inside a pNiO$_x$ NT. A lattice spacing of d = 0.249 nm is obtained, which corresponds to the (211) plane of $MAPbBr_3$. The inset of Figure 3c shows the corresponding FFT, which indicates the structure for the $MAPbBr_3$ formed inside the pNiO$_x$ NTs is polycrystalline in nature.

Figure 4 shows the XRD patterns taken from the $MAPbBr_3$ encapsulated in pNiO$_x$ NTs. The diffraction peaks from FTO glass substrate are labeled with triangles and those from nickel oxide are marked with black squares. $MAPbBr_3$ bulk materials usually have diffraction peaks at 2Θ=15.0°, 21.21°, 30.12°, 33.78°, 43.18° and 45.93° that correspond to the (100), (110), (200), (210), (220) and (300) planes, respectviely.[27] The encapsulated $MAPbBr_3$ samples show similar diffraction peaks but with different variations in peak intensity as compared with the bulk (Figure S12) because the bulk material has a characteristic square shape in morphology (Figure S10).

The stability of the $MAPbBr_3$ encapsulated inside pNiO$_x$ NTs was probed by XRD measurements made on freshly prepared

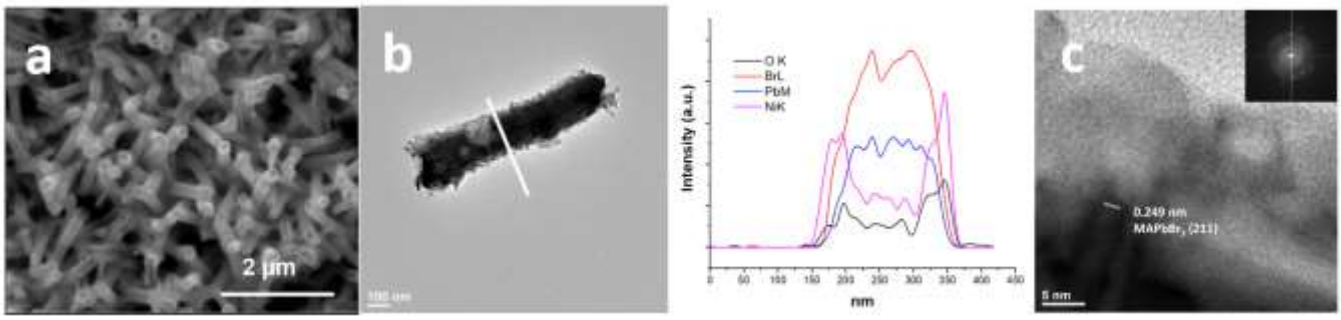

Figure 3. a) SEM image of $MAPbBr_3$ inside pNiO$_x$ NT arrays; b) TEM image of a MAPbBr3/pNiOx NT(left) and corresponding TEM-EDX line scan of NT (right); and c) HRTEM image of $MAPbBr_3$ inside a pNiO$_x$ NT and the corresponding FFT in the inset.

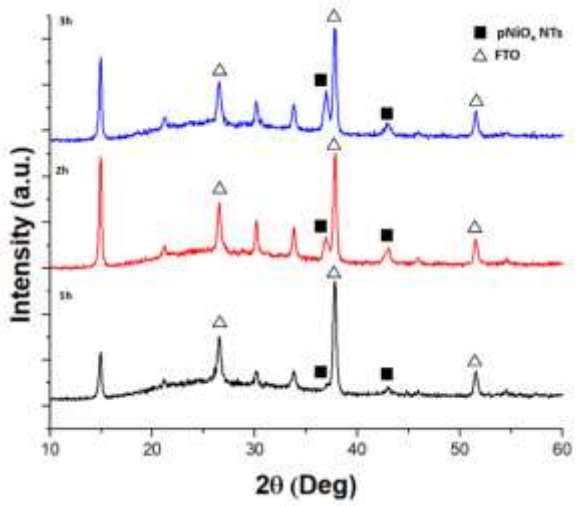

Figure 4. XRD of $MAPbBr_3$ encapsulated in $pNiO_x$ NTs with different tube wall thicknesses (growth time of 1, 2 and 3h) on glass substrates.

samples as well as those aged for a period of 3 months under ambient conditions (see XRD and PL Figure S13). The XRD pattern from the aged samples did not show any new peaks that are usually observed for degraded perovskites such as those from $PbBr_2$. The PL from the aged sample has the same peak position and line shape as that measured when the sample was freshly prepared. These results suggest that the $pNiO_x$ NTs provide protection for the $MAPbBr_3$ nanowires from degradation in air.

Both PL imaging and spectral measurements were taken on the encapsulated $MAPbBr_3$ in $pNiO_x$ NTs. **Figure 5a** shows the large area emission from $MAPbBr_3$ in $pNiO_x$ NTs with a tube wall nickel deposition time of 1 h. One can see that a very uniform green emission from the sample is observed, which is typical for $MAPbBr_3$. Figure 5b shows the corresponding PL spectrum with an emission peak at 540 nm. The insets of Figure 5b show the images of the sample under the room light and under the excitation of 375 nm laser, respectively. Similar PL images and spectra were obtained from $MAPbBr_3$ in $pNiO_x$ NTs with deposition times of 2 and 3 h as shown in Figures S14a-c. However, the PL emission intensities from these samples were found to be weak when compared to those with a tube wall deposition time of 1 h. This is most likely caused by the higher absorption of the tube walls with larger thicknesses. A blue shift of PL emission from 537 nm for bulk materials to 532 nm for the $MAPbBr_3$ in pNiOx NTs is observed. This blue shift is believed to be associated with quantum confinement effects in the encapsulated samples. The morphology differences of the $MAPbBr_3$ in $pNiO_x$ NTs and bulk $MAPbBr_3$ are shown by optical microscopy images in Figure S11.

In addition to PL measurements, LED devices were fabricated, and the electroluminescence was studied. For the first time, to the best of our knowledge, we achieved a novel electroluminescence device based on the configuration of FTO/TiO_2/$MAPbBr_3$-$pNiO_x$ NTs/Spiro-OMeTAD/Ag. In order to fabricate the LED devices, FTO substrates coated with a compact layer of TiO_2 were used. The anatase phase of TiO_2 layer was confirmed by Raman spectroscopy as shown in Figure S2. Raman peaks at 144 cm^{-1} (Eg), 397 cm^{-1} (B1g), 513/519 cm^{-1} (A1/B1g), and 639 cm^{-1} (Eg) were observed, which are characteristic modes for the anatase phase.[28]

NiO thin films have been well studied for applications in TiO_2-Perovskites-NiO solar cells.[29] However, it is not common to use NiO nanotubes for solar cells or LEDs. In this study, the LEDs were fabricated according to the diagram as shown in Figure S1. **Figure 6a** shows the device architecture and Figure 6b shows the band diagram, indicating the feasibility of charge separation and transport between the electrodes. The Spiro-OMeTAD and the $pNiO_x$ NTs serve as hole transport layers while the $pNiO_x$ NTs also serve as a template for the $MAPbBr_3$ nanowire formation. The TiO_2 is the hole blocking and electron transport layer. The electron-hole recombination occurs at the interface between NiO and $MAPbBr_3$. Both PL and EL were measured from the LED devices. Figure 6c shows the comparison of normalized PL and EL spectra. One can see that the EL peak is slightly shifted to a longer wavelength by about 5 nm with respect to the PL peak, with an EL peak located at 537 nm and PL at 532 nm. Figure 6d shows the EL of the LED device measured at different applied voltages. The inset is a photograph of the LED device when 6 V was applied, which confirms a uniform green emission from the device. At a voltage of 1 V, the EL intensity is very weak. As the applied voltage increases, the emission intensity increases rapidly up to about 4 V, where the increase slows and tends to saturate. The Comission Interationale de l'Eclairage (CIE) chromaticity coordinates at (0.249, 0.686) are shown in Figure 6e. The CIE coordinates are a measure of how close you are from white light as the standard natural white light (with coordinates at (0.33, 0.33)), and if the color is comfortable to the human eye. Figure 6f shows the semi logarithmic current density vs the voltage applied to the device. The current density tends to saturate after 6 V, which is consistent with the EL intensity saturation.

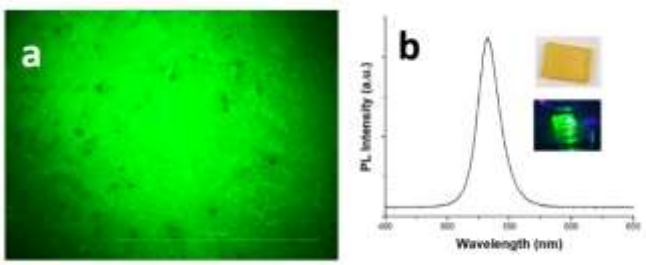

Figure 5. a) Microscopic PL image of $MAPbBr_3$ inside $pNiO_x$ NTs under fluorescence microscopy and b) the corresponding PL spectrum. Insets in b) shows the optical image of the sample under white light (top) and macroscopic PL image excited by 375 nm laser (bottom).

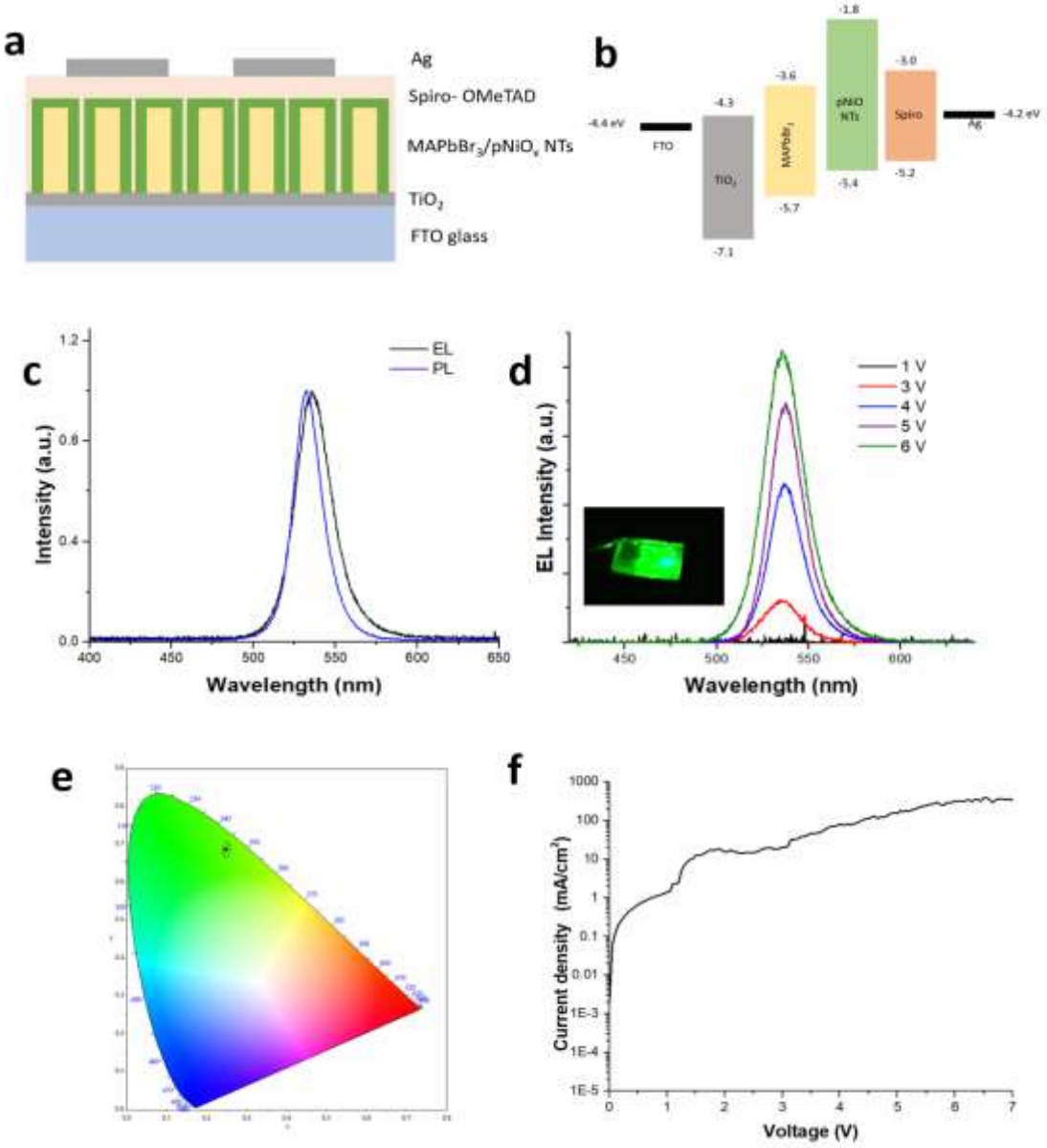

Figure 6. a) Structural diagram of the LED device; b) Energy diagram of the LED device; c) PL and EL spectra with normalized intensity; d) EL spectra measured at different applied voltages and the corresponding EL image in the inset; e) The corresponding CIE coordinates; and f) Current-Voltage plot of the LED device.

We also studied the electroluminescence efficiency and the current efficiency of the LEDs. The current efficiency is given by, η_{CE} =L/J, where L is the luminance and J is the current density. The external quantum efficiency η_{EQE} is defined as the number of photons emitted in the upper hemisphere to the number of injected charge carriers, and is given by the following equation: $\eta_{EQE}=P_{out}/P_{in}$.[30] Based on these equations we obtained a CE of 5.99 cd/A with an EQE of 3.9 %. These values are competitive among other perovskite-based LEDs with or without NiO_x in the architecture as compared in Table 1. Please note that our LED has perovskites in NTs while others were using planar LEDs. The NT shells are intended for stability improvement in device operation. Figure S15 shows EL intensity at different times to study the stability of the LED device. During the stability study, the device was kept in a desiccator for a certain number of hours and taken out for the EL intensity measurement at 5V. The EL intensity of the encapsulated perovskites drop by 50% after an operation of 150 hrs, probably due to the trapped charges inducing degradation in the perovskites.[31] The perovskite film prepared under the same conditions without capsulation shows an EL intensity drop to 30% of it's initial value after 150 hours. This comparison study shows that NiOx NTs improve the stability of the perovskites for light emitting devices. EL stability will be further studied by encapsulating perovskites in NiO_x NTs without pores and by the addition of an Al_2O_3 capping layer to protect the LED from moisture and air.

Table 1. comparison of LED performances with different device configurations

Device Structure	λ_{EL} peak (nm)	CE (cd/A)	EQE (%)	Ref
ITO/TiO_x (50 nm)/$MAPbBr_3$ (140 nm)/SPB-02T (10 nm)/Au (70 nm)	~530	0.22	0.051	[32]
ITO/PEDOT:PSS (40 nm)/$MAPbBr_3$ (30 nm)/TmPyPB (50 nm)/LiF (0.5 nm)/Al (100 nm)	~531	15.25	3.38	[33]
ITO/PEDOT:PSS/$MAPbBr_3$/SPW-111/LiF (1 nm)/Ag (80 nm)	~536	0.92	0.20	[34]
PEDOT:PSS:PFI (100 nm)/$MAPbBr_3$ (400 nm)/TPBi (50 nm)/LiF (1 nm)/Al (100 nm)	~540	42.9	8.53	[35]
ITO/$CsPbBr_3$/PEO/TPBi/FIrpic/Al	~520	2.9	--	[36]
ITO/NiO/TFB/PVK/$Cs_{0.7}FA_{0.3}PbBr_3MoO_x$/Au	~450	12	9.5	[37]
ITO/NiOx/$FAPbBr_3$/TPBi/LiF/Al	~540	12.1	2.59	[38]
ITO/NiOx/$MAPbBr_3$ (400 nm)/TPBi (50 nm)/LiF (1 nm)/Al (100 nm)	~540	15.9	--	[39]
FTO/TiO2/$MAPbBr_3$-NiO_x NTs/Spiro-OMeTAD/Ag	~542	5.99	3.9	This work

3. Conclusion

In this paper, we have demonstrated a novel method for making $pNiO_x$ NTs through the use of ZnO templates. We have shown the ability to control the shell thickness, inner diameter and length of these $pNiO_x$ NTs in a very precise way. For the first time, to the best of our knowledge, we have achieved a electroluminescence device using $MAPbBr_3$-$pNiO_x$ NTs. The process presented is inexpensive, scalable, compatible with current CMOS technology, and can be fabricated on a wide variety of substrates.

4. Experimental Section/Methods

4.1 Materials and Instrumentation

The following chemicals were purchased from Sigma-Aldrich and used as received without further purification: Zinc acetate $Zn(CH_3COO)_2{\cdot}2H_2O$, sodium hydroxide NaOH, methanol MeOH, ethanol EtOH, Acetic acid, Titanium Isopropoxide $Ti\{OCH(CH_3)_2\}_4$, zinc nitrate hexahydrate $Zn(NO_3)_2{\cdot}6H_2O$, hexamethylenetetramine HMTA, Nickel Chloride hexahydrate $NiCl_26H_2O$, Lead bromide $PbBr_2$, N^2,N^2,$N^{2'}$,$N^{2'}$,N^7,N^7,$N^{7'}$,$N^{7'}$-octakis(4-methoxyphenyl)-9,9'-spirobi9H-fluorene-2,2',7,7'-tetramine Spiro-OMeTAD, chlorobenzene, Dimethylformamide DMF. Methyl ammonium bromide MABr was from great solar.
Materials characterization was done by using scanning electron microscopy (SEM, FEI Quanta 200) with energy-dispersive X-ray spectroscopy (EDX), Transmission electron microscopy (TEM, JEOL JEM-2100), X-ray photoelectron spectroscopy (XPS, PHI 5000 Versaprobe Scanning XPS/UPS microscope), and RENISHAW Raman microscope with an excitation of 532 nm. Electrical characterization was done with a Keithley 4200 Semiconductor Analyzer and PL was taken by a fluorescence microscope with an excitation of 375 nm.

4.2 Fabrication of nickel oxide nanotubes

TiO_2 deposition: The FTO-coated glass was used as a substrate for device fabrication. Si wafers were also used in material deposition. The substrate was cleaned by 10% HCl for 1 hour followed by an additional ultrasonication cleaning in Acetone for 1 h. After that, the FTO glass and Si wafers were blow-dried. TiO_2 was deposited on the substrate by spin coating at 3,000 rpm with a solution containing Titanium Isopropoxide in 0.4M ethanol and 0.3 M acetic acid, which was followed by baking at 500 °C for 2 h.
Fabrication of Zinc oxide nanowire templates: ZnO nanocrystals (seeds) were prepared by mixing a solution of $Zn(CH_3COO)_2$ (12.5 mL, 0.01 M), MeOH (25 mL), and NaOH (6 mL, 0.03 M) at 60 °C for 2 h. ZnO seeds were deposited on substrates with spin-coating at 3000 rpm, followed by annealing at 300 °C for 1h. Then the ZnO nanowires were grown on the ZnO seed coated substrates by a hydrothermal process at 95 °C for 5 h using an aqueous solution of 0.06 M of $Zn(NO_3)_2$ and 0.06 M of HTMA .
Nickel oxide nanotube deposition: Nickel oxide coating was deposited by immersing ZnO NWs in $NiCl_2$ with a concentration of 1 M for 10 min to 3 h. Then the ZnO core was etched to form nickel oxide nanotubes by soaking the sample in 5M NaOH for 60 min. The NiO NTs were rinsed several times with DI H_2O followed by an annealing at 500 °C for 120 min, and finally the sample were rinsed with 1% HCl and rinsed several times with DI H_2O and dried in air.
Loading of $MAPbBr_3$ in nickel oxide nanotubes: Nickel oxide nanotube arrays were soaked in a DMF solution containing 200 mM MABr and $PbBr_2$ (1:1 molar ratio) at 60 °C for 2 h. The samples were then taken out of the solution and spun at 7000 rpm for 40 s to remove any excess reactant solution among the nanotube arrays, before finally being baked at 95 °C for 30 min.

4.3 Device fabrication and characterization

The fabrication of a typical LED device involves spin-coating of Spiro-OMeTAD onto the top of $MAPbBr_3$/nickel oxide nanotube arrays. Specifically, 72.3 mg Spiro-OMeTAD were dissolved in 1 ml chlorobenzene, and spin-coated on the nanotube arrays at 3000 rpm for 20 s. Then the sample was baked at 95 °C for 15 min. Finally, Ag contact was deposited onto Spiro-OMeTAD with a curing temperature of 95 °C for 15 min. The electrical and electroluminescence were characterized by using a Keithley 4200 Semiconductor Analyzer and a microscopic spectrometer.

Conflict of Interest

The authors declare no conflict of interest.

Author contributions

J. Cui directed and supervised the project. R. Gonzalez-Rodriguez initialized this project, fabricated and characterized the material/device. JL Coffer, E. Hathaway and Y. Lin were involved in the data analysis. All authors contributed to discussions and to finalizing the manuscript.

Acknowledgments

This work was supported by the U.S. National Science Foundation, grant number 2128367.

References

1

1. E. J. Juarez-Perez, R. S. Sanchez, L. Badia, G. Garcia-Belmonte, Y. S. Kang, I. Mora-Sero and J. Bisquert, *The Journal of Physical Chemistry Letters*, 2014, **5**, 2390-2394.
2. M. Zhang, F. Zhang, Y. Wang, L. Zhu, Y. Hu, Z. Lou, Y. Hou and F. Teng, *Scientific Reports*, 2018, **8**, 11157.
3. F. Fu, T. Feurer, Thomas P. Weiss, S. Pisoni, E. Avancini, C. Andres, S. Buecheler and Ayodhya N. Tiwari, *Nature Energy*, 2016, **2**, 16190.
4. X. He, P. Liu, S. Wu, Q. Liao, J. Yao and H. Fu, *Journal of Materials Chemistry C*, 2017, **5**, 12707-12713.
5. H. Wang, X. Zhang, Q. Wu, F. Cao, D. Yang, Y. Shang, Z. Ning, W. Zhang, W. Zheng, Y. Yan, S. V. Kershaw, L. Zhang, A. L. Rogach and X. Yang, *Nature Communications*, 2019, **10**, 665.
6. A. M. Streltsov, K. D. Moll, A. L. Gaeta, P. Kung, D. Walker and M. Razeghi, *Applied Physics Letters*, 1999, **75**, 3778-3780.
7. G. J. Gruber, W. W. Moses, S. E. Derenzo, N. W. Wang, E. Beuville and H. Ho, *IEEE Transactions on Nuclear Science*, 1998, **45**, 1063-1068.
8. W. Lee, J. Lee, H. Yun, J. Kim, J. Park, C. Choi, D. C. Kim, H. Seo, H. Lee, J. W. Yu, W. B. Lee and D.-H. Kim, *Advanced Materials*, 2017, **29**, 1702902.
9. C. Bao, J. Yang, S. Bai, W. Xu, Z. Yan, Q. Xu, J. Liu, W. Zhang and F. Gao, *Advanced Materials*, 2018, **30**, 1803422.
10. Y. Zhuang, W. Yuan, L. Qian, S. Chen and G. Shi, *Physical Chemistry Chemical Physics*, 2017, **19**, 12876-12881.
11. Z. Zhu, Q. Sun, Z. Zhang, J. Dai, G. Xing, S. Li, X. Huang and W. Huang, *Journal of Materials Chemistry C*, 2018, **6**, 10121-10137.
12. D. Ju, Y. Dang, Z. Zhu, H. Liu, C.-C. Chueh, X. Li, L. Wang, X. Hu, A. K. Y. Jen and X. Tao, *Chemistry of Materials*, 2018, **30**, 1556-1565.
13. Z. Zhang, M. Wang, L. Ren and K. Jin, *Scientific Reports*, 2017, **7**, 1918.
14. P.-C. Chen and S.-H. Yang, *ACS Applied Energy Materials*, 2019, **2**, 6705-6713.
15. T. Liu, K. Chen, Q. Hu, R. Zhu and Q. Gong, *Advanced Energy Materials*, 2016, **6**, 1600457.
16. D. Luo, L. Zhao, J. Wu, Q. Hu, Y. Zhang, Z. Xu, Y. Liu, T. Liu, K. Chen, W. Yang, W. Zhang, R. Zhu and Q. Gong, *Advanced Materials*, 2017, **29**, 1604758.
17. C.-G. Wu, C.-H. Chiang, Z.-L. Tseng, M. K. Nazeeruddin, A. Hagfeldt and M. Grätzel, *Energy & Environmental Science*, 2015, **8**, 2725-2733.
18. J. Zheng, L. Hu, J. S. Yun, M. Zhang, C. F. J. Lau, J. Bing, X. Deng, Q. Ma, Y. Cho, W. Fu, C. Chen, M. A. Green, S. Huang and A. W. Y. Ho-Baillie, *ACS Applied Energy Materials*, 2018, **1**, 561-570.
19. S. Bai, P. Da, C. Li, Z. Wang, Z. Yuan, F. Fu, M. Kawecki, X. Liu, N. Sakai, J. T.-W. Wang, S. Huettner, S. Buecheler, M. Fahlman, F. Gao and H. J. Snaith, *Nature*, 2019, **571**, 245-250.
20. K. T. P. Lim, C. Deakin, B. Ding, X. Bai, P. Griffin, T. Zhu, R. A. Oliver and D. Credgington, *APL Materials*, 2019, **7**, 021107.
21. R. Gonzalez-Rodriguez, N. Arad-Vosk, A. Sa'ar and J. L. Coffer, *The Journal of Physical Chemistry C*, 2018, **122**, 20040-20045.
22. Y. S. Chen, J. F. Kang, B. Chen, B. Gao, L. F. Liu, X. Y. Liu, Y. Y. Wang, L. Wu, H. Y. Yu, J. Y. Wang, Q. Chen and E. G. Wang, *Journal of Physics D: Applied Physics*, 2012, **45**, 065303.
23. D. Liu, D. Li and D. Yang, *AIP Advances*, 2017, **7**, 015028.
24. P. Salunkhe, M. A. A V and D. Kekuda, *Materials Research Express*, 2020, **7**, 016427.
25. J. H. Lee, Y. W. Noh, I. S. Jin, S. H. Park and J. W. Jung, *ACS Sustainable Chemistry & Engineering*, 2019, **7**, 15495-15503.
26. H. G. Gebretinsae, M. G. Tsegay and Z. Y. Nuru, *Materials Today: Proceedings*, 2021, **36**, 566-570.
27. K.-H. Wang, L.-C. Li, M. Shellaiah and K. Wen Sun, *Scientific Reports*, 2017, **7**, 13643.
28. S. Nezar, N. Saoula, S. Sali, M. Faiz, M. Mekki, N. A. Laoufi and N. Tabet, *Applied Surface Science*, 2017, **395**, 172-179.
29. A. Bashir, J. H. Lew, S. Shukla, D. Gupta, T. Baikie, S. Chakraborty, R. Patidar, A. Bruno, S. Mhaisalkar and Z. Akhter, *Solar Energy*, 2019, **182**, 225-236.
30. S.-H. Jeong, J. Park, T.-H. Han, F. Zhang, K. Zhu, J. S. Kim, M.-H. Park, M. O. Reese, S. Yoo and T.-W. Lee, *Joule*, 2020, **4**, 1206-1235.
31. N. Ahn, K. Kwak, M. S. Jang, H. Yoon, B. Y. Lee, J.-K. Lee, P. V. Pikhitsa, J. Byun and M. Choi, *Nature Communications*, 2016, **7**, 13422.
32. J. C. Yu, D. B. Kim, G. Baek, B. R. Lee, E. D. Jung, S. Lee, J. H. Chu, D.-K. Lee, K. J. Choi, S. Cho and M. H. Song, *Advanced Materials*, 2015, **27**, 3492-3500.

33. X. Zhao, B. Zhang, R. Zhao, B. Yao, X. Liu, J. Liu and Z. Xie, *The Journal of Physical Chemistry Letters*, 2016, **7**, 4259-4266.
34. J. C. Yu, D. W. Kim, D. B. Kim, E. D. Jung, J. H. Park, A.-Y. Lee, B. R. Lee, D. Di Nuzzo, R. H. Friend and M. H. Song, *Advanced Materials*, 2016, **28**, 6906-6913.
35. H. Cho, S.-H. Jeong, M.-H. Park, Y.-H. Kim, C. Wolf, C.-L. Lee, H. Heo Jin, A. Sadhanala, N. Myoung, S. Yoo, H. Im Sang, H. Friend Richard and T.-W. Lee, *Science*, 2015, **350**, 1222-1225.
36. C.-Y. Huang, S.-P. Chang, A. G. Ansay, Z.-H. Wang and C.-C. Yang, *Coatings*, 2020, **10**.
37. Y. Liu, J. Cui, K. Du, H. Tian, Z. He, Q. Zhou, Z. Yang, Y. Deng, D. Chen, X. Zuo, Y. Ren, L. Wang, H. Zhu, B. Zhao, D. Di, J. Wang, R. H. Friend and Y. Jin, *Nature Photonics*, 2019, **13**, 760-764.
38. S. Lee, D. B. Kim, I. Hamilton, M. Daboczi, Y. S. Nam, B. R. Lee, B. Zhao, C. H. Jang, R. H. Friend, J.-S. Kim and M. H. Song, *Advanced Science*, 2018, **5**, 1801350.
39. Y.-K. Chih, J.-C. Wang, R.-T. Yang, C.-C. Liu, Y.-C. Chang, Y.-S. Fu, W.-C. Lai, P. Chen, T.-C. Wen, Y.-C. Huang, C.-S. Tsao and T.-F. Guo, *Advanced Materials*, 2016, **28**, 8687-8694.